scientific reports

Check for updates

OPEN

Synthesis of patient-specific multipoint 4D flow MRI data of turbulent aortic flow downstream of stenotic valves

Pietro Dirix✉, Stefano Buoso, Eva S. Peper & Sebastian Kozerke

We propose to synthesize patient-specific 4D flow MRI datasets of turbulent flow paired with ground truth flow data to support training of inference methods. Turbulent blood flow is computed based on the Navier–Stokes equations with moving domains using realistic boundary conditions for aortic shapes, wall displacements and inlet velocities obtained from patient data. From the simulated flow, synthetic multipoint 4D flow MRI data is generated with user-defined spatiotemporal resolutions and reconstructed with a Bayesian approach to compute time-varying velocity and turbulence maps. For MRI data synthesis, a fixed hypothetical scan time budget is assumed and accordingly, changes to spatial resolution and time averaging result in corresponding scaling of signal-to-noise ratios (SNR). In this work, we focused on aortic stenotic flow and quantification of turbulent kinetic energy (TKE). Our results show that for spatial resolutions of 1.5 and 2.5 mm and time averaging of 5 ms as encountered in 4D flow MRI in practice, peak total turbulent kinetic energy downstream of a 50, 75 and 90% stenosis is overestimated by as much as 23, 15 and 14% (1.5 mm) and 38, 24 and 23% (2.5 mm), demonstrating the importance of paired ground truth and 4D flow MRI data for assessing accuracy and precision of turbulent flow inference using 4D flow MRI exams.

Aortic stenosis (AS) is a common condition associated with high morbidity and mortality[1,2]. Early detection and treatment of AS are associated with lower mortality rates, but the correct classification of the disease severity remains a challenge[2]. Since cardiovascular pathologies are usually associated with abnormal flow patterns[3–5] and irreversible pressure losses[6–10], the analysis of aortic flow fields is considered an important element for risk stratification and personalized planning of clinical interventions.

Cardiovascular magnetic resonance (CMR), and in particular phase-contrast (PC) MRI, has enabled measurements of time-resolved volumetric flow patterns (4D flow MRI)[11] in research and clinical settings. Despite recent advancements in sequence design[12–14] and image reconstruction methods[15], data is limited by spatiotemporal resolution and artifacts. Therefore, the development of robust and realistic models for the analysis of 4D flow MRI datasets is a fundamental step to enable predicting accuracy and precision of such measurements in research and clinical routine.

Deep learning (DL) methods are particularly suitable to discover intricate patterns in large datasets[16,17], which makes them ideal candidates to infer flow parameters and patterns contained in highly dimensional and complex 4D flow MRI exams. Recent works on image reconstruction[15], segmentation[18,19], classification[20] and flow super-resolution[21] have demonstrated the potential of DL algorithms. Berhane et al.[18] and Bratt et al.[19] used fully automated segmentation algorithms trained on manually labeled cine 2D and 4D flow MRI datasets to accelerate flow and diameter measurements in the aorta. However, the scarcity of high-quality labeled training datasets[22] effectively hampers the implementation of DL based inference approaches for 4D flow MRI. Fries et al.[20] alleviated the burden of obtaining manually labeled datasets by developing a weakly supervised DL model for classification of aortic valve malformations based on a small number of manually annotated scans. Other works have demonstrated the viability of augmenting clinical datasets using synthetic images[23,24] as the training of inference machines is significantly compromised by the limited number and potentially biased distributions of paired ground truth and imaging data. In general, however, the incorporation of manually labeled datasets as well as inherent uncertainties in the MRI measurements lead to biased and imperfect "ground truth" data. This

Institute for Biomedical Engineering, University and ETH Zurich, Zurich, Switzerland. ✉email: dirix@biomed.ee.ethz.ch

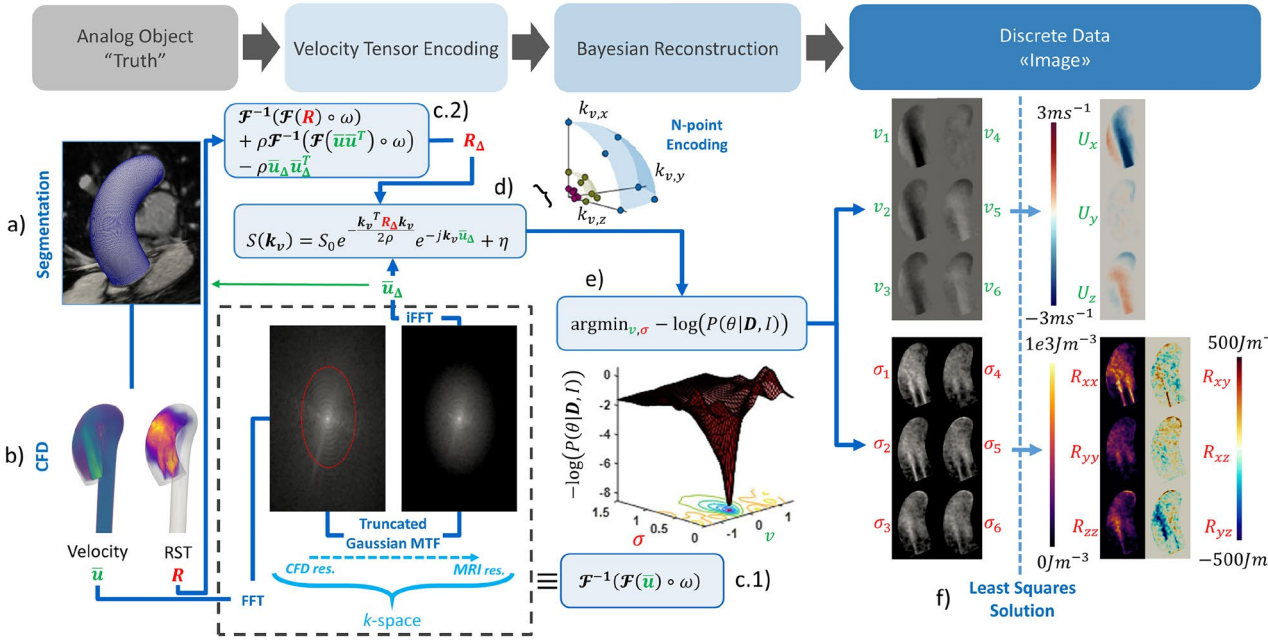

Figure 1. Pipeline for generation of synthetic patient-specific pulsatile mean and turbulent 4D flow MRI datasets. (**a**) Patient-specific segmentation and mesh generation. (**b**) Large Eddy Simulation CFD simulation to obtain mean velocity $\overline{u}$ and Reynolds shear tensor R. (**c**) Band-limited projection of velocity ($\overline{u}_\Delta$) and Reynolds stress tensor (R_Δ) in the spatial frequency domain (k-space) upon Fourier transform $\mathcal{F}$. (**d**) Signal model to generate MRI signal, S, for a given velocity encoding vector, $\boldsymbol{k_v}$, fluid density, ρ, and complex-valued white Gaussian noise, η. (**e**) Bayesian reconstruction of voxel mean velocities, v, and intra-voxel variances and co-variances, σ^2, and (**f**) their projection onto Cartesian coordinates using a least squares solution approach to obtain mean velocity vector U and Reynolds stress tensor R.

suggests that the intrinsic accuracy and precision of methods developed using such training datasets cannot be assessed and only approximate metrics can be derived using in-situ and in-vitro experiments[5].

Fluid flow can be obtained by simulating hemodynamics in realistic aortic shapes[25–27]. The corresponding MR signal is derived by simulating the acquisition process using the simulated data as input, effectively creating trustworthy ground truth and MR image pairs[21,28,29]. In Ferdian et al.[21], downsampled synthetic flow fields were derived from data generated by computational fluid dynamics (CFD) and used to train a super-resolution algorithm capable of estimating high-resolution flow features from low-resolution data. Inference was limited to velocity fields and turbulence was not incorporated. A more realistic approach consists of using data from CFD to compute the trajectories of individual material points while their complex-valued magnetization, and corresponding MRI signal, can be evaluated by solving the Bloch equations in the Lagrangian frame of reference[30,31]. Such a method can be used to evaluate specific MRI sequences while inherently accounting for flow-induced displacement and dephasing artifacts[32]. However, in order to accurately estimate MRI signals for turbulent flows, a large number of material points need to be tracked, rendering these simulations computationally expensive. Alternatively, synthetic MRI images can be obtained using a model equation for the signal, which directly includes pointwise velocity and turbulence data from CFD, drastically reducing the computational cost[33,34].

The presence of transitional or turbulent flow regimes downstream of aortic stenoses[5] suggests that simulations including turbulence modeling are an important step towards accurate modeling of pathological aortic flows. However, to the best of our knowledge, synthesis of 4D flow MRI data using turbulent flow simulations in realistic moving aortic shapes and signal encoding of velocity magnitude, phase and intra-voxel standard deviation (IVSD) has not been performed so far.

In this work we propose a framework to synthesize 4D flow MRI datasets of turbulent flow in the aorta with moving walls. Ground truth velocity and turbulence fields, computed with CFD, are input to generate multipoint MR signals at realistic resolution followed by Bayesian image reconstruction to output velocity and turbulence maps. The method is utilized with steady and pulsatile flow in idealized stenotic geometries to investigate the impact of the interplay of signal-to-noise ratio (SNR), spatial resolution and time averaging on measurement accuracy and precision of turbulent kinetic energy (TKE). Successively, patient-specific aortic 4D flow MRI data is generated with various degrees of aortic stenosis to report errors relative to ground truth for realistic SNR and resolutions.

Results

Synthetic 4D flow MRI data generation. Figure 1 illustrates the overall pipeline for the generation of synthetic 4D flow MRI data. 2D cine MRI and time-resolved 2D PC-MRI data are utilized to extract transient moving aortic geometries and corresponding inlet velocity profiles (Fig. 1a). A large eddy simulation (LES) CFD

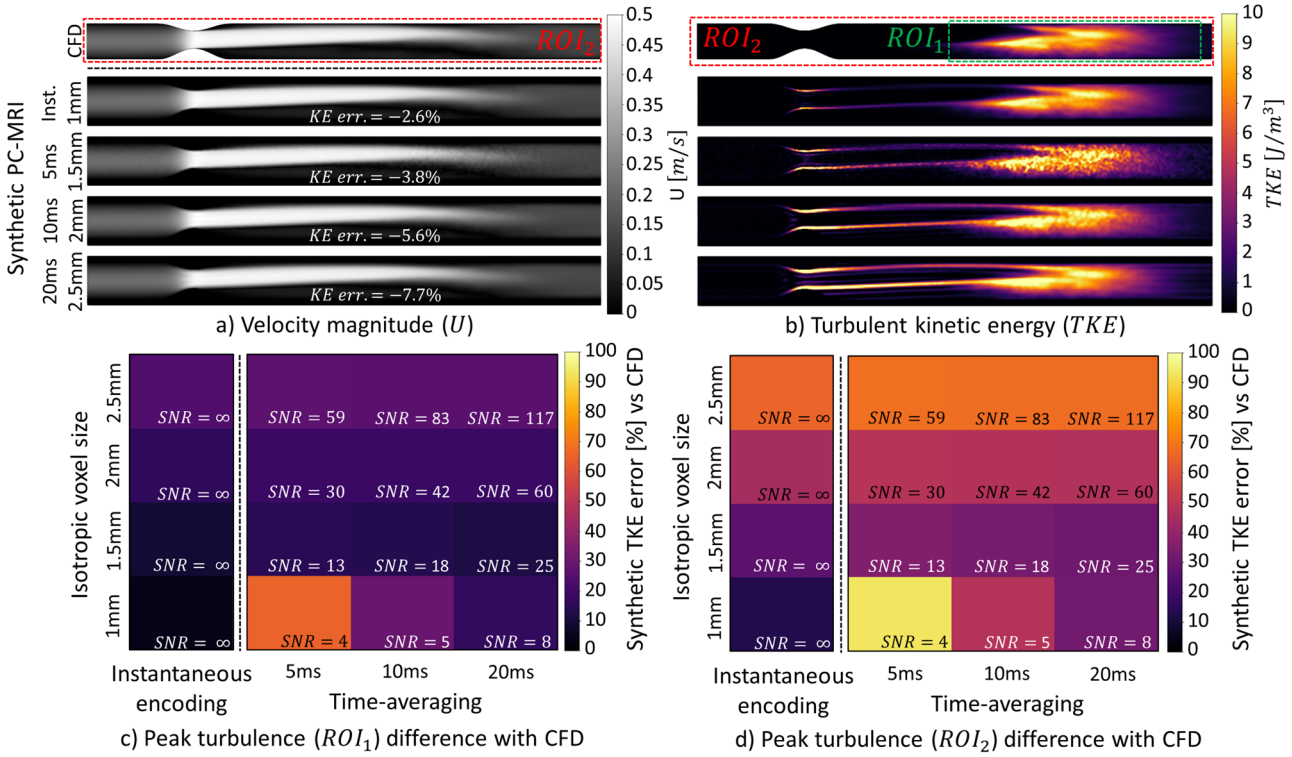

Figure 2. Impact of SNR and spatiotemporal resolution on velocity and turbulent kinetic energy for a 75% eccentric stenosis and steady flow. Magnitude of velocity (U) (**a**) and turbulent kinetic energy (TKE) (**b**) for varying voxel sizes, time averaging and, correspondingly, signal-to-noise ratios (SNR) are shown. The percentage error in total TKE as a function of spatial resolution, time averaging, and SNR is shown in (**c**) and (**d**) for ROI_1 (envelope of the turbulent region) and ROI_2 (whole geometry), respectively. Instantaneous (Inst.) encoding refers to a hypothetical noise-free PC-MRI experiment with infinitely high velocity encoding bandwidth.

approach with moving boundaries is employed to simulate turbulent flow (Fig. 1b). Subsequently, multipoint MRI signals are synthesized using dedicated signal models (Fig. 1c,d) followed by reconstruction using a Bayesian approach (Fig. 1e). Finally, velocity and intra-voxel standard deviation data are projected onto Cartesian coordinates to output velocity, Reynolds stress tensor (RST) and TKE maps (Fig. 1f). In this work both idealized and realistic shapes are used. The former allow to define control cases to study the effect of the interplay of SNR, resolution and time averaging for a given scan time budget, while the latter exemplify the utility of the method for patient-specific studies.

Spatiotemporal resolution and SNR dependencies in steady stenotic flow. In Fig. 2, the effect of spatial resolution and time averaging on velocity and TKE quantification for steady flow is visualized. Of note, a fixed hypothetical scan time budget is assumed in all MRI synthesis experiments and hence SNR $\propto V\sqrt{\Delta t}$, where V denotes voxel volume and Δt temporal averaging. For isotropic voxel sizes between 1 and 2.5 mm and hypothetical instantaneous encoding, total kinetic energy (KE) is underestimated by up to 8% while total TKE is overestimated by up to 24% in ROI_1 (envelope of the turbulent region, Fig. 2c) and by 13–65% for ROI_2 (whole geometry, Fig. 2d). For SNR values between 30 and 4, noise contribution to total TKE varies from 14 to 94% for ROI_1.

Spatiotemporal resolution and SNR dependencies in pulsatile stenotic flow. Figure 3 shows the effect of spatial resolution and time averaging on TKE quantification for pulsatile flow. For isotropic voxels sizes between 1 and 2.5 mm, total KE at peak systole is underestimated by up to 10% with hypothetical instantaneous encoding and by up to 22% when time averaging of 20 ms is assumed. A delay between peak systole and maximum total TKE is seen in the simulated data. Figure 3a shows that temporal and spatial gradients artificially contribute to up to 100% of measured TKE. This effect is also visible to a lesser extent at peak TKE in Fig. 3b, where up to 40% of the measured total TKE is erroneous. For instantaneous encoding with isotropic voxel sizes between 1 and 2.5 mm, total TKE is overestimated by up to 15% and 31% for ROI_1 (Fig. 3c) and ROI_2 (Fig. 3d), respectively. With 2.5 mm resolution and time averaging of 20 ms, total TKE is overestimated by up to 38% for ROI_1 and 58% for ROI_2.

Figure 4a,b compares total TKE during a simulated cardiac cycle for different settings of spatial resolution, time averaging and SNR. Figure 4c,d visualize the effect of spatial resolution and time averaging on the quantification of total TKE integrated over the cardiac cycle. Isotropic spatial resolutions between 1.5 and 2 mm and

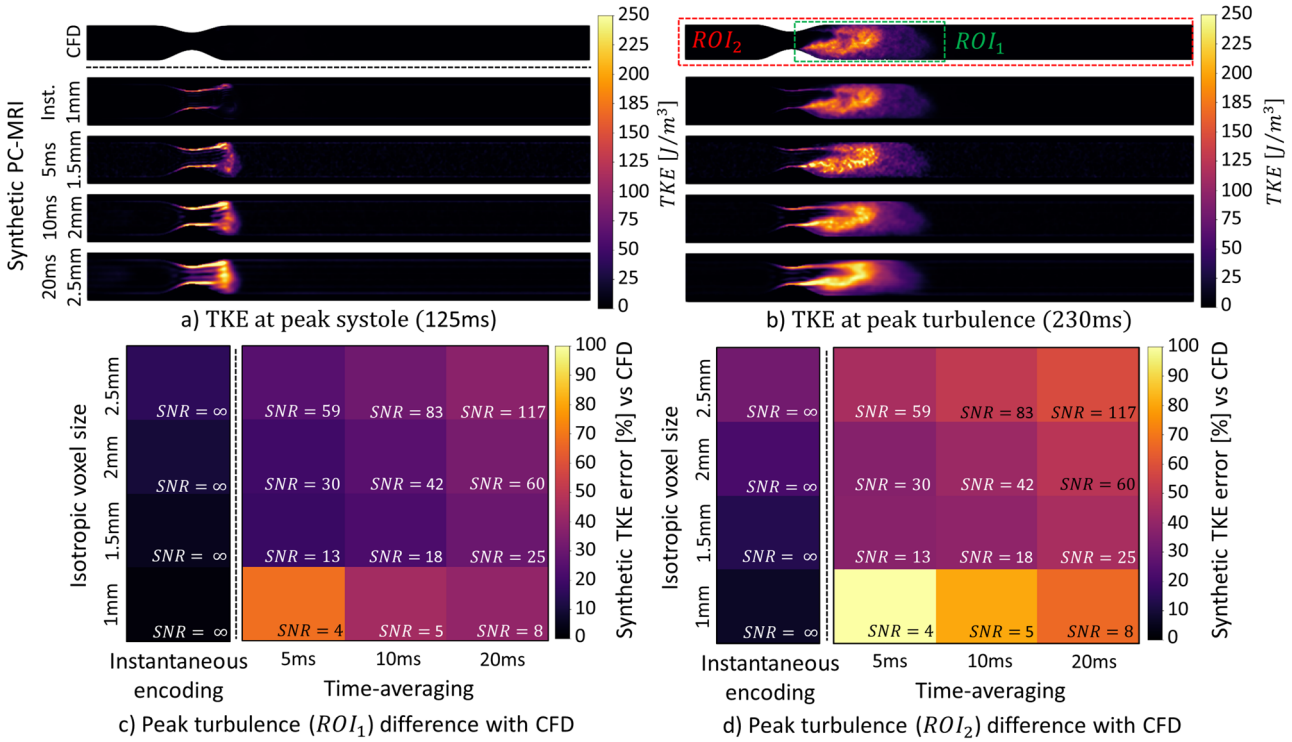

Figure 3. Impact of SNR and spatiotemporal resolution on turbulent kinetic energy for a 75% eccentric stenosis and pulsatile flow. Turbulent kinetic energy at peak systole (**a**) and at peak total TKE (**b**) is shown. Percentage errors of peak total TKE are compared in (**c**) and (**d**) for ROI_1 (envelope of the turbulent region) and ROI_2 (whole geometry). Instantaneous (Inst.) encoding refers to a hypothetical noise-free PC-MRI experiment with infinitely high velocity encoding bandwidth.

time averaging of 5 ms lead to overestimation of total TKE by up to 26% for ROI_1 (Fig. 4c) and 70% for ROI_2 (Fig. 4d), respectively.

Patient-specific velocity and turbulence fields. Figure 5 compares velocity magnitude and TKE maps at peak systole and peak TKE for CFD and synthetic PC-MRI. Artificially high TKE values are visible at the walls and in flow regions with high velocity gradients.

Figure 6a shows the evolution of TKE for various degrees of stenosis during the cardiac cycle. Peak TKE occurs after peak systole with a delay δ that depends on the stenosis degree. For stenotic degrees of 50%, 75% and 90% the delay δ is 32, 53 and 90 ms. For mild to severe aortic stenosis, peak total TKE varies from 7 to 70 mJ. Figure 6b summarizes peak TKE statistics.

Mean and standard deviation of TKE in the ascending aorta for stenotic degrees of 50, 75 and 90% are overestimated by 37.9, 8.6 and 8.6% and 13.5, 5.0 and 13.3%, respectively, for a voxel size of 1.5 mm. Similarly, the overestimation is 55.2, 18.2 and 16.7% and 23.1, 12.5 and 23.8% for a voxel size of 2.5 mm (Fig. 6b). Higher spatial resolution results in outliers with larger TKE.

The patient-specific datasets presented in this work required on average 60 wall-clock hours using 48 cores to obtain the CFD solution, each time frame was around 260 MB.

Discussion

In this study, a framework for the synthesis of time-resolved multipoint 4D flow MRI data of turbulent flow in patient-specific, moving aortic geometries has been presented. The impact of spatial resolution, time averaging and SNR was investigated for both steady and pulsatile flows in idealized geometries for a fixed hypothetical scan time budget.

The qualitative comparison of velocity and TKE maps in Fig. 2a,b–d confirmed that turbulence measurements are more sensitive to SNR and spatial resolution when compared to velocity measurements and that the ROI used to compute total TKE should be selected carefully. In Fig. 2c,d, limited spatial resolution and low SNR both contribute to overestimation of TKE due to contributions by noise and spatial velocity gradients in accordance with previous studies[35,36]. Variations in total TKE for different time averaging in Fig. 2c,d are due to SNR differences, as time averaging has no influence for steady flows.

Contributions by temporal velocity gradients further increase the artificial overestimation of TKE in pulsatile flows as demonstrated in Fig. 3a. Turbulence only appears after peak systole in the ground truth, suggesting TKE production is kick-started by post-systolic flow deceleration (Fig. 4a).

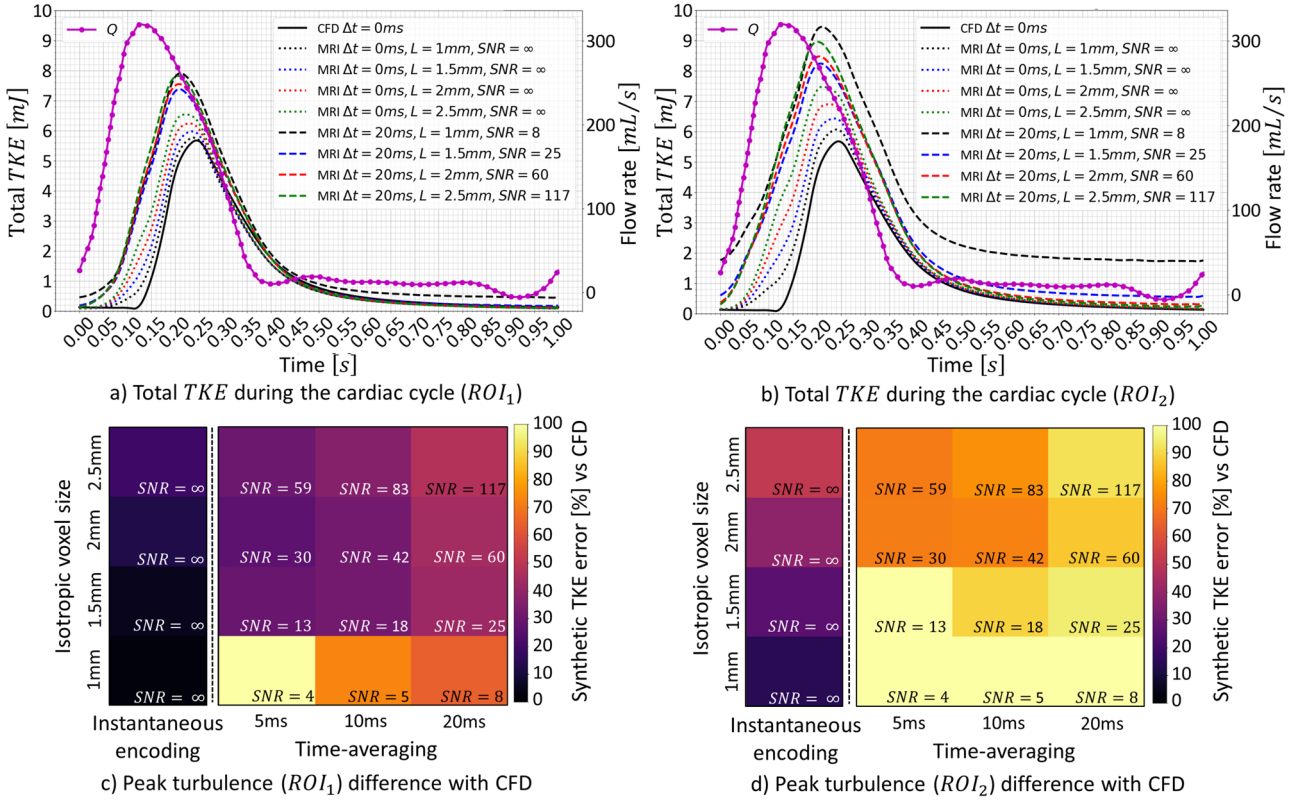

Figure 4. Impact of SNR and spatiotemporal resolution on time-resolved turbulent kinetic energy for a 75% eccentric stenosis and pulsatile flow. Time-resolved total TKE and flow rate (Q) during a simulated cardiac cycle for varying voxel sizes (L), time averaging (Δt) and, correspondingly, signal-to-noise ratios (SNR) for ROI_1 (**a**) and ROI_2 (**b**) (see Fig. 3). Errors in total TKE integrated during the cardiac cycle ROI_1 (**c**) and ROI_2 (**d**). Instantaneous ($\Delta t = 0$ ms) encoding refers to a hypothetical noise-free PC-MRI experiment with infinitely high velocity encoding bandwidth.

Spatial and temporal gradients compromise measured velocity and TKE values in voxels due to partial volume effects, which are visible at the walls of the aorta, where artificially high TKE values are present. In particular, we have demonstrated that, at peak systole, the measured RST is purely artificial and does not represent turbulence (Fig. 3a). Additionally, we have observed that peak TKE occurs with a delay compared to peak systole, suggesting that TKE quantification at peak systole as proposed in the literature may need to be reconsidered[33].

For spatial resolutions of 1.5 and 2.5 mm and time averaging of 5 ms, peak total TKE downstream of a 75% stenosis is overestimated by 15 and 24%, respectively (Fig. 6a). Similar overestimations (18 and 25%) were observed using the idealized geometry with pulsatile flow, suggesting that observations in Figs. 2, 3 and 4 can be extrapolated to more realistic geometries and flows. Higher spatial resolution creates outliers with larger TKE values due to lower SNR levels. For a typical 4D flow MRI isotropic spatial resolution of 2.5 mm and stenotic degree > 75%, voxel-wise TKE is consistently overestimated in the ascending aorta, suggesting that 4D flow MRI overestimation of TKE might be predictable for high turbulence regimes.

In the present study, net flow was identical for the different degrees of simulated stenoses. Since pressure along the aorta depends on the stenotic degree, variations in vessel cross-sectional area are expected, which were not modeled in our work. Future work is warranted to integrate wall displacements resulting from the interaction of flow and wall compliance to arrive at realistic pulse wave velocities. Full fluid–structure interaction approaches, or reduced order models applied to the elastic and viscoelastic response of the tissue could be translated from our previous works[37–40]. Also, anatomical variability could be augmented using anatomical models based on low rank reconstructions[41].

Another limitation of the present study relates to the use of a simplified approach for generating PC-MRI signals, assuming ideal encoding and readout and, therefore, neglecting the impact of encoding schemes on measured values of velocity and turbulence. Flow-induced displacement artifacts were not included, and cycle-to-cycle variations were condensed into cycle-averaged quantities. These assumptions were made to reduce the computational cost as compared to more accurate modelling of the imaging processes[31]. Recent work from Dillinger et al.[42] demonstrates that the implementation of realistic encoding gradients in an Eulerian–Lagrangian Bloch solver results in systematic underestimation of high frequency components of turbulence. Therefore, quantification of in-vivo turbulence is subject to overestimation due to partial volume effects on one hand and underestimation due to band-limited velocity encoding gradients on the other hand.

The study also lacks comparison between in-vivo and synthetic 4D flow MRI datasets. However, due to the complexity of flow patterns in the aorta and assumptions used in patient-specific CFD, only a qualitative

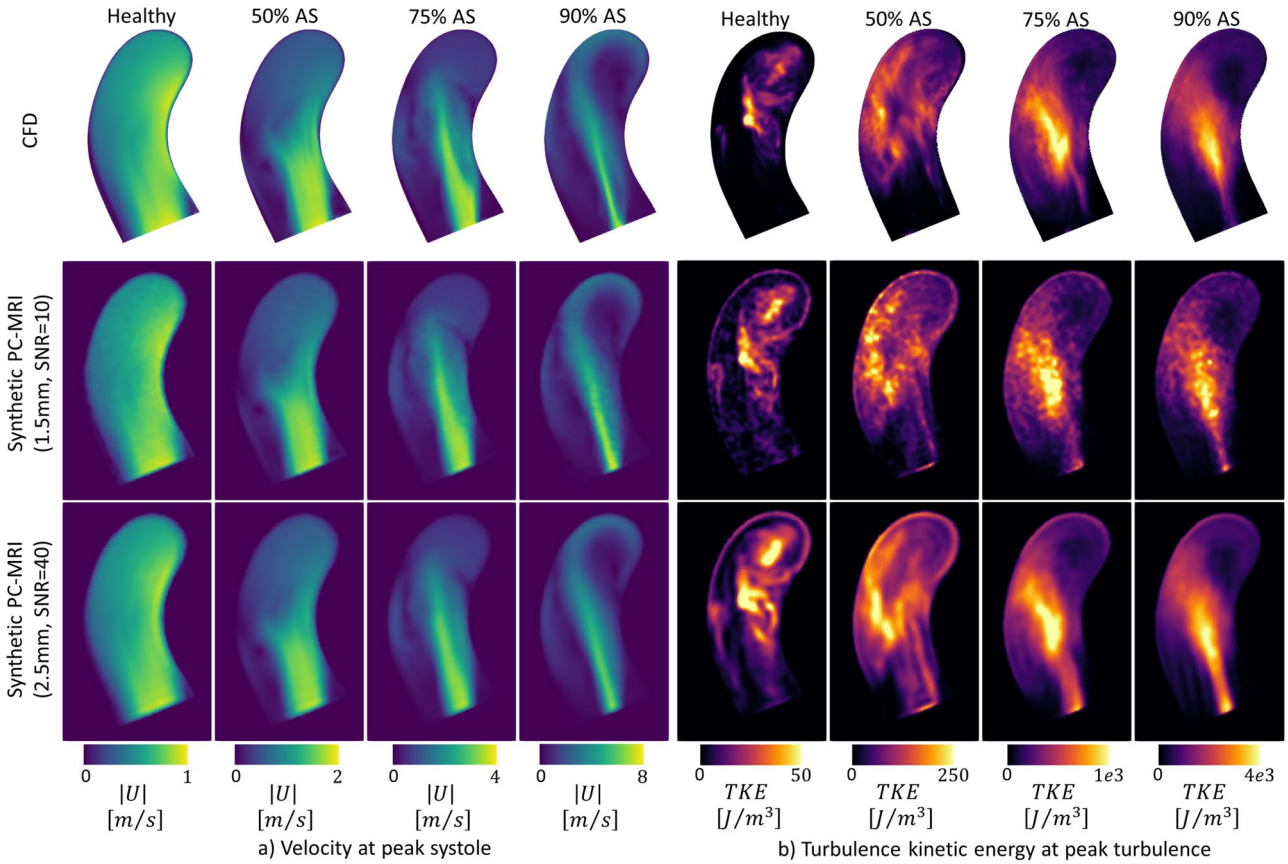

Figure 5. Patient-specific velocity and TKE maps for varying degrees of stenosis (foot-head slices of the aorta aligned with the inflow jet). (**a**) Magnitude of the velocity at peak systole and (**b**) turbulent kinetic energy at peak total TKE for two resolutions and the corresponding reference CFD. For (**a**) and (**b**), from left to right, healthy inlet flow and simulated stenosis degrees of 50%, 75% and 90% are shown. Note the difference in color bar scaling for both velocity and TKE depending on the stenosis degree. A video showing all time steps is available in the online supplemental material.

comparison of flow patterns would be achievable[26,43,44]. Although this is a general limitation for patient-specific simulations, it does not directly affect our proposed workflow as our aim is to generate realistic flows in the aorta rather than to attempt to duplicate patient-specific hemodynamics in every detail.

To conclude, the synthesis framework presented here enables the generation of paired sets of patient-specific realistic ground truth and 4D flow MRI data to cater to training of deep learning algorithms for image reconstruction[15] and inference[21] in the future. Although this work focused on velocity and TKE in post-stenotic aortic flows, the ground truth CFD contains information about pressure drop, wall shear stresses and pulse wave velocity, opening the door to the possibility of analyzing other important hemodynamic biomarkers in future works. Additionally, the patient-specific nature of this work suggests that, if adequate datasets are available, the pipeline could be used to generate synthetic 4D flow datasets for other valvular or aortic pathologies, such as aortic regurgitation (AR), bicuspid aortic valve (BAV) and dilated ascending aorta.

Methods

Idealized computational domain. An eccentric stenotic tube with fixed walls and stenosis severity of 75%[45,46] was modeled as idealized geometry. This geometry has been widely studied in the literature[34,47,48] and has an analytical description with the stenosis modelled as a cosine function offset in one direction by an eccentricity of 5% of the diameter. The stenosis throat was positioned at a distance of 3 diameters from the inlet, and the cylinder extended for 20 diameters downstream. A structured hexahedral butterfly mesh with 2.7 M cells was generated using OpenFoam's blockMesh utility[49].

Patient-specific computational domain. Realistic aortic geometries were obtained from in-vivo MRI data. The subjects were studied upon written informed consent under the approval of the ethics committee of the Canton of Zurich, Switzerland, and according to institutional guidelines. Imaging experiments were performed on a 1.5 T MR system (Philips Healthcare, Best, The Netherlands) using a 32-channel receive array. High-resolution cine balanced steady-state free precession slices ($1 \times 1 \times 5$ mm^3) were acquired orthogonally to the aorta centerline with a temporal resolution of 40 frames/cardiac cycle in a breath hold. A total of 9 slices were distributed uniformly along the aortic center line, covering the aortic arch and the descending aorta with the first slice positioned at the aortic root. Lumen boundaries were extracted and the corresponding 3D surface extrapo-

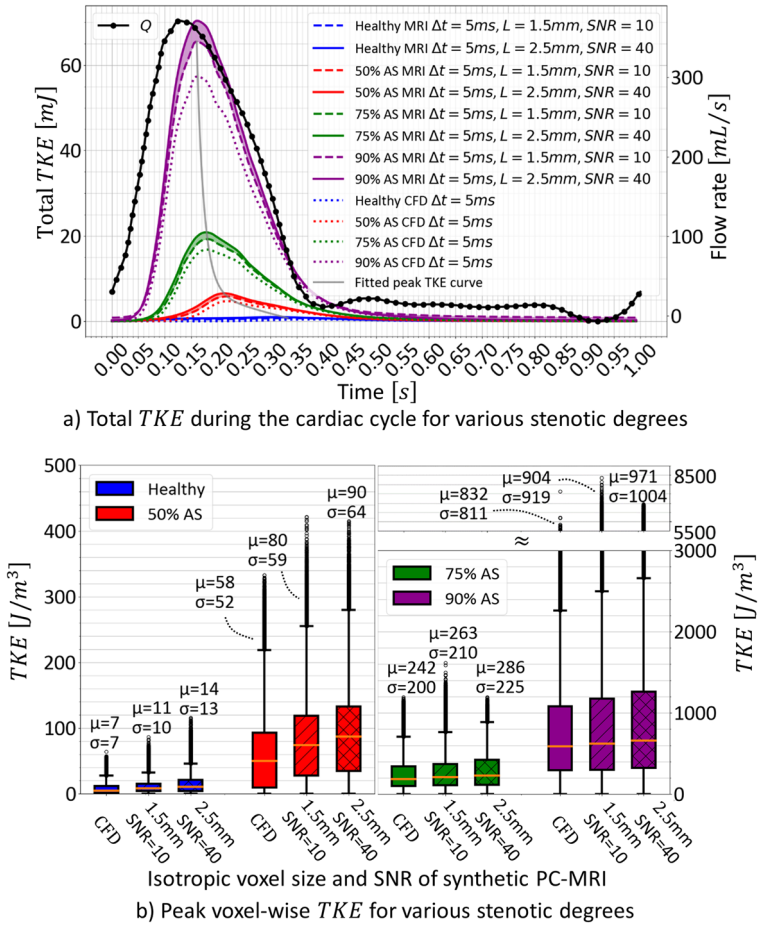

Figure 6. Variations in turbulent kinetic energy depending on the stenosis degree during the cardiac cycle and at peak total TKE. (**a**) Comparison of measured total TKE for two resolutions of PC-MRI and the reference CFD during the cardiac cycle for a healthy inlet flow and simulated aortic stenosis degrees of 50%, 75% and 90%. Note the temporal lag between peak flow rate and peak TKE represented by the fitted peak TKE curve. (**b**) Mean μ and standard deviation σ of peak voxel-wise TKE for the two resolutions of PC-MRI for healthy flow and 50%, 75% and 90% stenoses.

lated from segmented 2D contours (Supplemental Fig. S1). The brachiocephalic, left common carotid and left subclavian arteries were removed, as their impact on flow features in the ascending aorta is not significant[50]. A structured hexahedral butterfly mesh was then generated using OpenFoam's blockMesh utility[49] on the anatomy at end diastole, which was considered as the initial phase of the cardiac cycle (Fig. 1a). A mesh size of 2.2 M cells with mean and maximum cell heights in the region of interest of 0.37 mm and 0.6 mm was found to be sufficient to accurately simulate both velocity and turbulence fields in aortae with pathological inflows[51–53].

Boundary conditions. Fully developed Hagen-Poiseuille profiles were used as inlet boundary conditions for the idealized geometries. The mean inlet Reynolds number (*Re*) was set to 1000 for both steady and pulsatile scenarios. For the pulsatile case, the velocity waveform was extracted from in-vivo data acquired at the aortic root in a healthy subject with a peak inlet *Re* of 4000, typical for physiological flows[54].

Aortic wall motion for the patient-specific simulation was extracted for all cardiac phases and was used as boundary condition for the CFD simulation. Time-resolved inlet velocity profiles for the patient-specific simulations were extracted from time-resolved 2D PC MRI spoiled gradient echo imaging ($1.5 \times 1.5 \times 8$ mm^3, 40 frames/cardiac cycle). Pathological stenotic inlets were generated by projecting the healthy inlet velocities onto reduced cross sections (50, 75 and 90%) of the geometrical model inlet while keeping the flow rate constant (Supplemental Fig. S2).

Computational fluid dynamics. Blood flow in the aorta was computed using the three-dimensional, unsteady and incompressible Navier–Stokes (NS) equations in moving domains. Blood was assumed Newtonian and incompressible with density $\rho = 1060$ kg/m^3 and kinematic viscosity $\mu = 3.5e^{-3}$ Pa s[55]. In our work, the NS equations were solved using a large eddy simulation (LES) model in the arbitrary Lagrangian–Eulerian (ALE) framework as implemented in OpenFOAM® v1806[49]. The subgrid scheme selected was the wall-adapting local-

eddy viscosity (WALE) subgrid-scale (SGS) model[51,52] and Spalding's wall function was used[56]. Second-order central differences and backward Euler schemes were used for spatial and temporal discretization. Adaptive time stepping was used to reduce simulation times; at peak turbulent production the time step ranged between 25 and 100 µs depending on the stenotic degree[7,34] (Fig. 1b). Simulations were run on a high-performance cluster of the Swiss National Supercomputing Center (CSCS). On average 6 wall clock hours per cardiac cycle were required using 48 cores (300 CPU hours) for a simulation of moderate aortic stenosis.

Computation of the Reynolds stress tensor. The covariance matrix $Cov(\boldsymbol{u})$ of N measurements of a time varying velocity vector $\boldsymbol{u} = (\boldsymbol{u}_1, \boldsymbol{u}_2, \ldots, \boldsymbol{u}_N) \in \mathbb{R}^{3\times N}$ is defined as:

$$Cov(\boldsymbol{u}) = \frac{1}{N}\sum_{n=1}^{N}(\boldsymbol{u_n} - \overline{\boldsymbol{u}})(\boldsymbol{u_n} - \overline{\boldsymbol{u}})^{\mathrm{T}} = \overline{\boldsymbol{u}'\boldsymbol{u}'^{T}} = \rho^{-1}\boldsymbol{R} \tag{1}$$

where $\bar{\blacksquare}$ is the averaging operator, $\boldsymbol{u}' = \boldsymbol{u} - \overline{\boldsymbol{u}}$ are the velocity fluctuations over the mean velocity $\overline{\boldsymbol{u}}$, $\boldsymbol{u}'\boldsymbol{u}'^{T} = \boldsymbol{u}' \otimes \boldsymbol{u}'$ defines an outer product, and $\boldsymbol{R} \in \mathbb{R}^{3\times 3}$ is the Reynolds stress tensor. In the case of pulsatile flow, the N measurements $(\boldsymbol{u}_1, \boldsymbol{u}_2, \ldots, \boldsymbol{u}_N)$ are acquired at the same time t_0 of the cycle, over N cycles. Due to band-limited encoding and finite readout times in MRI, flow measurements are not instantaneous snapshots, but include flow information over finite durations. To model this condition, measurements of $\overline{\boldsymbol{u}}$ and $\boldsymbol{R}$ are performed in a temporal window Δt around t_0, where Δt corresponds to the modeled temporal averaging duration of the acquisition.

Synthetic 4D flow MRI. The MR signal S^*, assuming Gaussian intra-voxel velocity distribution (IVSD) of variance σ_{k_v} reads (Fig. 1d):

$$S^*(\boldsymbol{k_{v,i}}) = S_0 \mathrm{e}^{-\frac{\sigma^2_{k_{v,i}}|\boldsymbol{k_{v,i}}|^2}{2}} \mathrm{e}^{-j\boldsymbol{k_{v,i}}\overline{\boldsymbol{u}}_{\boldsymbol{\Delta}}} + \eta \tag{2}$$

where $\boldsymbol{k_{v,i}} = k_{v,i}\overrightarrow{\boldsymbol{e}}_i = \left[k_{vx}, k_{vy}, k_{vz}\right]_i \in \mathbb{R}^{1\times 3}$ represents flow sensitivity along the ith direction with encoding velocity frequency $k_{v,i} = \pi/[\mathrm{VENC}]_i$. $\eta \propto \mathrm{SNR}$ is complex Gaussian noise with zero mean and standard deviation $\sigma_\eta = \left|\overline{S}_{ROI}\right| \cdot (\mathrm{SNR})^{-1}$ with $\overline{S}_{ROI}$ being the mean noise-free signal in the region of interest, defined as the full fluid domain for all simulations. S_0 is the normalized reference signal without velocity encoding that in this work is modelled as:

$$S_0 = \frac{1}{2}\left[\left(\frac{|\overline{\boldsymbol{u}}_{\boldsymbol{\Delta}}|}{|\overline{\boldsymbol{u}}_{\boldsymbol{\Delta}}|_{max}}\right)^{\frac{1}{3}} + 1\right] \tag{3}$$

where $\overline{\boldsymbol{u}}_{\boldsymbol{\Delta}}$ is the velocity field at the selected MR signal resolution. The term $\sigma^2_{k_{v,i}}\left|\boldsymbol{k_{v,i}}\right|^2$ can be expressed as $\rho^{-1}\boldsymbol{k_{v,i}}\boldsymbol{R}^{\boldsymbol{t}}_{\boldsymbol{\Delta}}\boldsymbol{k_{v,i}}^{\mathrm{T}}$ where $\boldsymbol{R}^{\boldsymbol{t}}_{\boldsymbol{\Delta}}$ is the Reynolds stress tensor at the selected MR resolution Δ_L. Both $\boldsymbol{R}^{\boldsymbol{t}}_{\boldsymbol{\Delta}}$ and $\overline{\boldsymbol{u}}_{\boldsymbol{\Delta}}$ are obtained by first projecting computed values from the CFD simulations onto a regular grid $(n_x \times n_y \times n_z)$ with isotropic voxel size $L = 0.65$ mm. The fields are subsequently downsampled to the prescribed MR resolution, Δ_L, by apodization with a truncated 3D Gaussian modular transfer function (MTF) ω with standard deviation $\sigma_G = \sqrt{8\ln 2}L/\Delta_\mathrm{L}$. The truncation window is a box with width $w \propto L/\Delta_\mathrm{L}$, such that the Gaussian MTF is truncated at an amplitude of 0.5 along each principal Cartesian direction. The downsampled RST $\boldsymbol{R}^{\boldsymbol{t}}_{\boldsymbol{\Delta}}$ and velocity $\overline{\boldsymbol{u}}_{\boldsymbol{\Delta}}$ are then defined as (Fig. 1c.1 and c.2):

$$\overline{\boldsymbol{u}}_{\boldsymbol{\Delta}} = \mathcal{F}^{-1}(\mathcal{F}(\overline{\boldsymbol{u}}) \circ \omega) \tag{4}$$

$$\boldsymbol{R}^{\boldsymbol{t}}_{\boldsymbol{\Delta}} = \mathcal{F}^{-1}\left(\mathcal{F}\left(\boldsymbol{R}^{\boldsymbol{t}}\right) \circ \omega\right) + \rho\mathcal{F}^{-1}\left(\mathcal{F}\left(\overline{\boldsymbol{u}\boldsymbol{u}}^{\boldsymbol{T}}\right) \circ \omega\right) - \rho\overline{\boldsymbol{u}}_{\boldsymbol{\Delta}}\overline{\boldsymbol{u}}^{\boldsymbol{T}}_{\boldsymbol{\Delta}} \tag{5}$$

where $\mathcal{F}$ is the Fourier operator and $\circ$ is the apodization operator. Synthetic noise was defined for the idealized geometries (Figs. 2, 3 and 4) as a function of voxel volume V and temporal averaging of signal Δt (analogous to the repetition time TR assuming that signal is continuously acquired during this time) as $\mathrm{SNR} = \alpha V\sqrt{\Delta t}$, where $\alpha = 1.68$ is a scaling factor designed to obtain $SNR = 30$ for $V = 2 \times 2 \times 2$ mm^3 and $\Delta t = 5$ ms.

Reynolds stress tensor reconstruction. The RST can be determined by encoding along six non-collinear directions and solving a system of linear equations. For six measurements along six different velocity encoding directions $\{i | i \in \mathbb{Z}, 1 \le i \le 6\}$, $\sigma_{k_{v,i}}$ is obtained from the ratio between $S^*(\boldsymbol{k_{v,i}})$ and $S^*(0)$ as:

$$\sigma^2_{k_{v,i}} = \frac{2}{\left|\boldsymbol{k_{v,i}}\right|^2}\ln\frac{|S^*(0)|}{\left|S^*(\boldsymbol{k_{v,i}})\right|} \approx \frac{\boldsymbol{k_{v,i}}^{\boldsymbol{T}}\boldsymbol{R}^*\boldsymbol{k_{v,i}}}{\rho\left|\boldsymbol{k_{v,i}}\right|^2} \tag{6}$$

where $\boldsymbol{R}^*$ is the estimated RST. By rewriting Eq. (6), the following system of linear equations is obtained:

$$\sigma^2_{k_{v,i}} = \frac{1}{\rho\left|\boldsymbol{k_{v,i}}\right|^2}(k^2_{vx,i}, k^2_{vy,i}, k^2_{vz,i}, 2k_{vx,i}k_{vy,i}, 2k_{vx,i}k_{vz,i}, 2k_{vy,i}k_{vz,i}) \cdot \left(R_{xx}, R_{yy}, R_{zz}, R_{xy}, R_{xz}, R_{yz}\right)^T = \boldsymbol{H_i}(\boldsymbol{k_{v,i}}, \rho)\boldsymbol{r}^* \tag{7}$$

where $\boldsymbol{\sigma}_{\boldsymbol{k_v}} \in \mathbb{R}^{6\times1}$ is the IVSD vector, $\boldsymbol{H_i}\left(\boldsymbol{k_{v,i}}, \rho\right)$ is the ith row of $\boldsymbol{H}(\boldsymbol{k_v}, \rho) \in \mathbb{R}^{6\times6}$, a transformation matrix that depends on $\boldsymbol{k_v} \in \mathbb{R}^{6\times3}$ and ρ, and $\boldsymbol{r^*} \in \mathbb{R}^{6\times1}$ is the vector representation of the symmetric RST tensor $\boldsymbol{R^*}$. The encoding matrix $\boldsymbol{k_v}$ was designed for orthogonal encoding[35,57] in this study, but can be modified for any other encoding scheme. The elements of the RST can be calculated voxel-wise using the pseudoinverse (Fig. 1f):

$$\boldsymbol{r^*} = \left(\boldsymbol{H}^{\mathrm{T}}\boldsymbol{H}\right)^{-1}\boldsymbol{H}^{\mathrm{T}}\boldsymbol{\sigma}^2_{\boldsymbol{k_v}} \tag{8}$$

The symmetric RST vector $\boldsymbol{r^*}$ can be recast into its tensor representation $\boldsymbol{R^*} \in \mathbb{R}^{3\times3}$. The elements along the diagonal represent velocity fluctuation variances while the off-diagonal elements represent covariances. Turbulent kinetic energy in [J/m^3] is then defined as:

$$\mathrm{TKE} = 1/2\ \mathrm{Tr}\left(\boldsymbol{R^*}\right) \tag{9}$$

where $\mathrm{Tr}(\boldsymbol{R^*})$ is the trace of the RST. Total TKE in [mJ] refers to the volumetric integration of TKE in a region of interest.

Velocity reconstruction. Redundant encoding schemes provide additional information for estimation of mean velocities. The velocities encoded in the six directions are defined by $\breve{\boldsymbol{v}} = \arg\left(S^*\left(\boldsymbol{k_{v,i}}\right)\right) \in \mathbb{R}^{6\times1}$ and can be written as:

$$\breve{v}_i = \boldsymbol{k_{v,i}}\left|\boldsymbol{k_{v,i}}\right|^{-1}\boldsymbol{u^*} = \boldsymbol{K_i}\left(\boldsymbol{k_{v,i}}\right)\boldsymbol{u^*} \tag{10}$$

where $\boldsymbol{K_i}\left(\boldsymbol{k_{v,i}}\right)$ is the ith row of $\boldsymbol{K}(\boldsymbol{k_v}) \in \mathbb{R}^{6\times3}$, the normalized encoding tensor and $\boldsymbol{u^*} \in \mathbb{R}^{3\times1}$ is the Cartesian velocity vector. A solution to this overdetermined system of linear equations is provided by the pseudo-inverse (Fig. 1f):

$$\boldsymbol{u^*} = \left(\boldsymbol{K}^{\mathrm{T}}\boldsymbol{K}\right)^{-1}\boldsymbol{K}^{\mathrm{T}}\breve{\boldsymbol{v}} \tag{11}$$

From the Cartesian velocity vector $\boldsymbol{u^*}$, kinetic energy (KE) in [J/m^3] is defined as:

$$\mathrm{KE} = \frac{\rho}{2}\left|\boldsymbol{u^*}\right|^2 \tag{12}$$

Total KE in [mJ] refers to the volumetric integration of KE in a region of interest.

Bayesian reconstruction. Turbulence estimation shows high sensitivity within a limited range of IVSD values dictated by the choice of velocity encoding (VENC) and, respectively, encoding strength $k_v = \pi/\mathrm{VENC}$. This suggests that single VENC acquisitions are limited in their ability to probe the rich variety of expected IVSD in pathological aortic flows[12]. To mitigate this effect, a multipoint approach was used to probe velocity and turbulence fields using orthogonal encoding with three different encoding strengths[35] (Supplemental Table S1). For each encoding direction, the acquisitions at different encoding strengths were combined using Bayesian multipoint unfolding[12] to generate a set of directional velocities $\breve{v}_i$ and IVSD $\sigma_{k_v \cdot i}$ that were then converted to velocities and RST using Eqs. (8 and 11).

Data availability

Our Python code for 4D flow MRI synthesis and Bayesian reconstruction is publicly available (https://gitlab.ethz.ch/ibt-cmr-public/4dflowmrisynthesis), accompanied with demo data corresponding to the idealized geometry with pulsatile flow presented in Fig. 3b).

Received: 23 June 2022; Accepted: 8 September 2022
Published online: 26 September 2022

References

1. Dweck, M. R., Boon, N. A. & Newby, D. E. Calcific aortic stenosis. *J. Am. Coll. Cardiol.* **60**, 1854–1863 (2012).
2. Thoenes, M. *et al.* Patient screening for early detection of aortic stenosis (AS)—Review of current practice and future perspectives. *J. Thorac. Dis.* **10**, 5584–5594 (2018).
3. Saitta, S. *et al.* Evaluation of 4D flow MRI-based non-invasive pressure assessment in aortic coarctations. *J. Biomech.* **94**, 13–21 (2019).
4. Feneis, J. F. *et al.* 4D flow MRI quantification of mitral and tricuspid regurgitation: Reproducibility and consistency relative to conventional MRI. *J. Magn. Reson. Imaging* **48**, 1147–1158 (2018).
5. Garcia, J., Barker, A. J. & Markl, M. The role of imaging of flow patterns by 4D flow MRI in aortic stenosis. *JACC Cardiovasc. Imaging* **12**, 252–266 (2019).
6. Dyverfeldt, P., Hope, M. D., Tseng, E. E. & Saloner, D. Magnetic resonance measurement of turbulent kinetic energy for the estimation of irreversible pressure loss in aortic stenosis. *JACC Cardiovasc. Imaging* **6**, 64–71 (2013).
7. Ha, H. *et al.* Estimating the irreversible pressure drop across a stenosis by quantifying turbulence production using 4D Flow MRI. *Sci. Rep.* **7**, 1–14 (2017).
8. Marlevi, D. *et al.* Non-invasive estimation of relative pressure in turbulent flow using virtual work-energy. *Med. Image Anal.* **60**, 101627 (2020).
9. Binter, C. *et al.* Turbulent kinetic energy assessed by multipoint 4-dimensional flow magnetic resonance imaging provides additional information relative to echocardiography for the determination of aortic stenosis severity. *Circ. Cardiovasc. Imaging* **10**, e005486 (2017).

10. Zhuang, B., Sirajuddin, A., Zhao, S. & Lu, M. The role of 4D flow MRI for clinical applications in cardiovascular disease: current status and future perspectives. *Quant. Imaging Med. Surg.* **11**, 4193–4210 (2021).
11. Markl, M., Frydrychowicz, A., Kozerke, S., Hope, M. & Wieben, O. 4D flow MRI. *J. Magn. Reson. Imaging* **36**, 1015–1036 (2012).
12. Binter, C., Knobloch, V., Manka, R., Sigfridsson, A. & Kozerke, S. Bayesian multipoint velocity encoding for concurrent flow and turbulence mapping. *Magn. Reson. Med.* **69**, 1337–1345 (2013).
13. Ma, L. E. *et al.* Aortic 4D flow MRI in 2 minutes using compressed sensing, respiratory controlled adaptive k-space reordering, and inline reconstruction. *Magn. Reson. Med.* **81**, 3675–3690 (2019).
14. Wiesemann, S. *et al.* Impact of sequence type and field strength (1.5, 3, and 7T) on 4D flow MRI hemodynamic aortic parameters in healthy volunteers. *Magn. Reson. Med.* **85**, 721–733 (2021).
15. Vishnevskiy, V., Walheim, J. & Kozerke, S. Deep variational network for rapid 4D flow MRI reconstruction. *Nat. Mach. Intell.* **2**, 228–235 (2020).
16. Lundervold, A. S. & Lundervold, A. An overview of deep learning in medical imaging focusing on MRI. *Z. Med. Phys.* **29**, 102–127 (2019).
17. Leiner, T. *et al.* Machine learning in cardiovascular magnetic resonance: basic concepts and applications. *J. Cardiovasc. Magn. Reson.* **21**, 61 (2019).
18. Berhane, H. *et al.* Fully automated 3D aortic segmentation of 4D flow MRI for hemodynamic analysis using deep learning. *Magn. Reson. Med.* **84**, 2204–2218 (2020).
19. Bratt, A. *et al.* Machine learning derived segmentation of phase velocity encoded cardiovascular magnetic resonance for fully automated aortic flow quantification. *J. Cardiovasc. Magn. Reson.* **21**, 1 (2019).
20. Fries, J. A. *et al.* Weakly supervised classification of aortic valve malformations using unlabeled cardiac MRI sequences. *Nat. Commun.* **10**, 3111 (2019).
21. Ferdian, E. *et al.* 4DFlowNet: Super-resolution 4D flow MRI using deep learning and computational fluid dynamics. *Front. Phys.* **8**, (2020).
22. Ravi, D. *et al.* Deep learning for health informatics. *IEEE J. Biomed. Heal. Inform.* **21**, 4–21 (2017).
23. Shin, H.-C. *et al. Medical Image Synthesis for Data Augmentation and Anonymization Using Generative Adversarial Networks*, 1–11 (2018) https://doi.org/10.1007/978-3-030-00536-8_1.
24. Duchateau, N., Sermesant, M., Delingette, H. & Ayache, N. Model-based generation of large databases of cardiac images: synthesis of pathological cine MR sequences from real healthy cases. *IEEE Trans. Med. Imaging* **37**, 755–766 (2018).
25. Leuprecht, A., Perktold, K., Kozerke, S. & Boesiger, P. Combined CFD and MRI study of blood flow in a human ascending aorta model. *Biorheology* **39**, 425–429 (2002).
26. Miyazaki, S. *et al.* Validation of numerical simulation methods in aortic arch using 4D Flow MRI. *Heart Vessels* **32**, 1032–1044 (2017).
27. Romarowski, R. M., Lefieux, A., Morganti, S., Veneziani, A. & Auricchio, F. Patient-specific CFD modelling in the thoracic aorta with PC-MRI–based boundary conditions: A least-square three-element Windkessel approach. *Int. J. Numer. Method. Biomed. Eng.* **34**, 1–21 (2018).
28. Bakhshinejad, A. *et al.* Merging computational fluid dynamics and 4D Flow MRI using proper orthogonal decomposition and ridge regression. *J. Biomech.* **58**, 162–173 (2017).
29. Töger, J. *et al.* Blood flow imaging by optimal matching of computational fluid dynamics to 4D-flow data. *Magn. Reson. Med.* **84**, 2231–2245 (2020).
30. Petersson, S., Dyverfeldt, P., Gårdhagen, R., Karlsson, M. & Ebbers, T. Simulation of phase contrast MRI of turbulent flow. *Magn. Reson. Med.* **64**, 1039–1046 (2010).
31. Puiseux, T., Sewonu, A., Moreno, R., Mendez, S. & Nicoud, F. Numerical simulation of time-resolved 3D phase-contrast magnetic resonance imaging. *PLoS ONE* **16**, e0248816 (2021).
32. Steinman, D. A., Ethier, C. R. & Rutt, B. K. Combined analysis of spatial and velocity displacement artifacts in phase contrast measurements of complex flows. *J. Magn. Reson. Imaging* **7**, 339–346 (1997).
33. Ha, H. *et al.* Estimation of turbulent kinetic energy using 4D phase-contrast MRI: Effect of scan parameters and target vessel size. *Magn. Reson. Imaging* **34**, 715–723 (2016).
34. Ha, H. *et al.* Assessment of turbulent viscous stress using ICOSA 4D Flow MRI for prediction of hemodynamic blood damage. *Sci. Rep.* **6**, 1–14 (2016).
35. Walheim, J., Dillinger, H., Gotschy, A. & Kozerke, S. 5D flow tensor MRI to efficiently map reynolds stresses of aortic blood flow in-vivo. *Sci. Rep.* **9**, 1–12 (2019).
36. Binter, C., Gülan, U., Holzner, M. & Kozerke, S. On the accuracy of viscous and turbulent loss quantification in stenotic aortic flow using phase-contrast MRI. *Magn. Reson. Med.* **76**, 191–196 (2016).
37. Buoso, S. & Palacios, R. On-demand aerodynamics in integrally actuated membranes with feedback control. *AIAA J.* **55**, 377–388 (2017).
38. Buoso, S., Dickinson, B. T. & Palacios, R. Bat-inspired integrally actuated membrane wings with leading-edge sensing. *Bioinspir. Biomim.* **13**, 016013 (2017).
39. Buoso, S. & Palacios, R. Electro-aeromechanical modelling of actuated membrane wings. *J. Fluids Struct.* **58**, 188–202 (2015).
40. Buoso, S. & Palacios, R. Viscoelastic effects in the aeromechanics of actuated elastomeric membrane wings. *J. Fluids Struct.* **63**, 40–56 (2016).
41. Buoso, S., Joyce, T. & Kozerke, S. Personalising left-ventricular biophysical models of the heart using parametric physics-informed neural networks. *Med. Image Anal.* **71**, 102066 (2021).
42. Dillinger, H., McGrath, C., Guenthner, C. & Kozerke, S. Fundamentals of turbulent flow spectrum imaging. *Magn. Reson. Med.* https://doi.org/10.1002/mrm.29001 (2021).
43. Nannini, G. *et al.* Aortic hemodynamics assessment prior and after valve sparing reconstruction: A patient-specific 4D flow-based FSI model. *Comput. Biol. Med.* **135**, 104581 (2021).
44. Roldán-Alzate, A. *et al.* Hemodynamic study of TCPC using in vivo and in vitro 4D Flow MRI and numerical simulation. *J. Biomech.* **48**, 1325–1330 (2015).
45. Varghese, S. S., Frankel, S. H. & Fischer, P. F. Direct numerical simulation of stenotic flows. Part 1. Steady flow. *J. Fluid Mech.* **582**, 253–280 (2007).
46. Varghese, S. S., Frankel, S. H. & Fischer, P. F. Direct numerical simulation of stenotic flows. Part 2. Pulsatile flow. *J. Fluid Mech.* **582**, 281–318 (2007).
47. Tan, F. P. P., Wood, N. B., Tabor, G. & Xu, X. Y. Comparison of les of steady transitional flow in an idealized stenosed axisymmetric artery model with a RANS transitional model. *J. Biomech. Eng.* **133**, 1–12 (2011).
48. Varghese, S. S., Frankel, S. H. & Fischer, P. F. Modeling transition to turbulence in eccentric stenotic flows. *J. Biomech. Eng.* **130**, 1–7 (2008).
49. OpenFOAM Foundation Inc. OpenFOAM v1806. https://www.openfoam.com/ (2018).
50. Liu, X. *et al.* A numerical study on the flow of blood and the transport of LDL in the human aorta: The physiological significance of the helical flow in the aortic arch. *Am. J. Physiol. Heart Circ. Physiol.* **297**, 163–170 (2009).
51. Andersson, M., Lantz, J., Ebbers, T. & Karlsson, M. Quantitative assessment of turbulence and flow eccentricity in an aortic coarctation: impact of virtual interventions. *Cardiovasc. Eng. Technol.* **6**, 281–293 (2015).

52. Manchester, E. L. *et al.* Analysis of turbulence effects in a patient-specific aorta with aortic valve stenosis. *Cardiovasc. Eng. Technol.* **12**, 438–453 (2021).
53. Pirola, S. *et al.* Computational study of aortic hemodynamics for patients with an abnormal aortic valve: The importance of secondary flow at the ascending aorta inlet. *APL Bioeng.* **2**, 026101 (2018).
54. Stalder, A. F. *et al.* Assessment of flow instabilities in the healthy aorta using flow-sensitive MRI. *J. Magn. Reson. Imaging* **33**, 839–846 (2011).
55. Buoso, S. *et al.* Reduced-order modeling of blood flow for noninvasive functional evaluation of coronary artery disease. *Biomech. Model. Mechanobiol.* **18**, 1867–1881 (2019).
56. Spalding, D. B. A single formula for the "law of the wall". *J. Appl. Mech. Trans. ASME* **28**, 455–458 (1960).
57. Hasan, K. M., Parker, D. L. & Alexander, A. L. Comparison of gradient encoding schemes for diffusion-tensor MRI. *J. Magn. Reson. Imaging* **13**, 769–780 (2001).

Acknowledgements

This work was supported by funding from the Swiss National Science Foundation (SNSF), grant CR23I3_166485. The Swiss National Supercomputing Center (CSCS) is acknowledged for providing computational resources.

Author contributions

P.D., S.B. and S.K. designed the study and discussed the results; P.D. and S.B. developed the simulation framework; E.P. acquired the in-vivo scans; All authors participated in revising the manuscript and read and approved the final manuscript.

Competing interests

The authors declare no competing interests.

Additional information

Supplementary Information The online version contains supplementary material available at https://doi.org/10.1038/s41598-022-20121-x.

Correspondence and requests for materials should be addressed to P.D.

Reprints and permissions information is available at www.nature.com/reprints.

Publisher's note Springer Nature remains neutral with regard to jurisdictional claims in published maps and institutional affiliations.